

Nanostructured Hypoeutectic Fe-B Alloy Prepared by a Self-propagating High Temperature Synthesis Combining a Rapid Cooling Technique

Licai Fu · Jun Yang · Qinling Bi · Weimin Liu

Received: 8 September 2008 / Accepted: 17 October 2008 / Published online: 6 November 2008
© to the authors 2008

Abstract We have successfully synthesized bulk nanostructured Fe_{94.3}B_{5.7} alloy using the one-step approach of a self-propagating high temperature synthesis (SHS) combining a rapid cooling technique. This method is convenient, low in cost, and capable of being scaled up for processing the bulk nanostructured materials. The solidification microstructure is composed of a relatively coarse, uniformly distributed dendrite to a nanostructured eutectic matrix with α -Fe(B) and *t*-Fe₂B phases. The fine eutectic structure is disorganized, and the precipitation Fe₂B is found in the α -Fe(B) phase of the eutectic. The dendrite phase has the *t*-Fe₂B structure rather than α -Fe(B) in the Fe_{94.3}B_{5.7} alloy, because the growth velocity of *t*-Fe₂B is faster than that of the α -Fe with the deeply super-cooling degree. The coercivity (H_c) and saturation magnetization (M_s) values of the Fe_{94.3}B_{5.7} alloy are 11 A/m and 1.74T, respectively. Moreover, the Fe_{94.3}B_{5.7} alloy yields at 1430 MPa and fractures at 1710 MPa with a large ductility of 19.8% at compressive test.

Keywords Nanostructured eutectic · Fe_{94.3}B_{5.7} alloy · Self-propagating high temperature synthesis (SHS) · Soft magnetic performance · Mechanical behavior

Introduction

Nanostructured materials have been shown to exhibit outstanding high strength and hardness, corrosion resistance, good soft magnetic performance, and other unusual properties [1–5]. For establishing meaningful correlations between the structure and properties, it is necessary to have fully dense, artifact-free, and well-characterized samples. A number of prepared methods of bulk nanostructured materials have been investigated in the recent decades [6–10]. These processes usually use a two-step approach including the synthesis of nano powder and particles and their subsequent consolidation by hot isostatic pressing, shock compression, powder sintering, etc, or a one-step approach such as electrodeposition, devitrification of amorphous and severe plastic deformation. In the two-step approach, the materials often suffer from porosity, contamination, and weak bonding resulted to low ductility, whereas the one-step approaches are limited to the synthesis of small-scale products. Therefore, it is of interest to develop new processes that are convenient, low in cost, and capable of being scaled up for tailoring the nanostructured materials, for instance a self-propagating high temperature synthesis (SHS) technique [11–13].

The Fe-B alloy system is of interest in several fields of engineering materials. This system shows a significant glass forming ability (GFA) for compositions close to the Fe-rich eutectic [14, 15]. Nanostructured Fe-B alloy is usually obtained from the metallic materials [16, 17]. The stable phase Fe₂B and metastable phase Fe₃B often coexist in the nanostructured Fe-B alloy. The thermal stability of the nanostructured Fe-B alloy is reduced greatly because the metastable phase Fe₃B transforms into the equilibrium phase mixture of α -Fe and Fe₂B at 840 °C [18]. In this paper, we have successfully synthesized bulk nanostructured

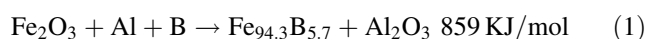
L. Fu · J. Yang (✉) · Q. Bi · W. Liu
State Key Laboratory of Solid Lubrication, Lanzhou Institute of Chemical Physics, Chinese Academy of Sciences,
Lanzhou 730000, People's Republic of China
e-mail: jyang@lzb.ac.cn

L. Fu
Graduate University of Chinese Academy of Sciences,
Beijing 100039, People's Republic of China
e-mail: tyflc@163.com

Fe_{94.3}B_{5.7} alloy making use of the one-step approach of an SHS combining a rapid cooling technique that is convenient, low in cost, and capable of being scaled up for tailoring bulk nanostructured materials [11–13, 19]. The nanostructured Fe_{94.3}B_{5.7} alloy is only composed of α -Fe(B) and *t*-Fe₂B phases. It possesses good soft magnetic performance and excellent mechanical behavior.

Experimental

The aluminothermic reaction was designed as expressed in Eq. 1. The reactant of ferric sesquioxide, aluminum, and boron powders were dry-mixed for 8 h in a hard steel vial with Al₂O₃ spheres, and then about 80 g of the mixed powders were cold-pressed in a copper mold (70 mm in the diameter) under a uniaxial pressure of 50 MPa. The characteristics of the reactant powders are given in Table 1. Three grams of Al, S, and MnO₂ powder mixture in the mass ratio of 1:1:1 was pressed into a pellet with dimensions of 15 mm (diameter) \times 4 mm. The pellet was put on top of the pressed reactant powders as an igniter.



The copper mold with the reactants was placed in an SHS reactor as described in the literature [19–21]. The reactor was purged with argon gas at room temperature, heated to 180 °C, and then purged for a second time. Heating of the reactor continued after introducing of 7 MPa of argon gas. The reaction of the igniter was started when the reactor reached 260 °C, which results in an instantaneous release of a large amount of heat that ignites the aluminothermic reaction and the synthesis reaction was subsequently finished in a few seconds. The products were kept in the reactor under argon gas pressure to cool down.

After cooling to room temperature, the products were taken out of the reactor. The resulting Fe_{94.3}B_{5.7} alloy was about 5 mm thick and 30 mm in diameter. The black Al₂O₃ product was on top of the target product, which separated naturally from the desired Fe_{94.3}B_{5.7} alloy and could be removed by hand. The Fe_{94.3}B_{5.7} alloys prepared in the repeated experiments have the same phases, nanostructure, and properties as those mentioned below, which indicates that the processing is stable and can be conveniently reproduced.

Table 1 Properties of the raw material powders

Powder	Size (mesh)	Purity (wt%)	Impurity
Fe ₂ O ₃	100	≥ 99	Cl ⁻ , SO ₄ ²⁻ , Cu, N
Al	100–200	≥ 99	Fe, Si, Cu, H ₂ O
B	amorphous	≥ 99	–

The polished cross sections were investigated with X-ray diffractometry (XRD, Philips X'per) using CuK α radiation. The samples before and after compressive test were observed with a JSM-5600LV scanning electron microscope (SEM). Several specimens punched from the cross sections of the products were electrochemically thinned in an electrolyte of nine parts of methanol and one part of perchloric acid with twin-jet electropolish at –30 °C and were examined using a JEM-1200EX transmission electron microscope (TEM) with a magnetically shielded object lens pole-piece operated at 120 kV. The differential scanning calorimeter (DSC, STA 449 C) was employed to evaluate the phase transformations in Ar atmosphere with the heating and cooling rates of 20 °C/min. The saturation magnetization and coercive forces were tested using a vibrating sample magnetometer (VSM, 7304, USA) equipped with a 1.0 T magnet and the measurements were conducted at room temperature. The cylindrical compressive specimens with a dimension of \varnothing 3 mm \times 4.5 mm were cut using an electrodischarging machine, and the specimen surfaces were polished with a 1,000-grit emery paper. A quasi-static uniaxial compressive test was performed at room temperature with a crosshead speed of $6 \times 10^{-4} \text{ s}^{-1}$. In order to minimize friction effects, the specimen–die interfaces were lubricated with graphite.

Results and Discussion

The chemical reaction of the igniter is initiated at about 260 °C in the SHS reactor and instantaneously releases large heat, which ignites the reaction of the reactants. Then combustion wave of the reaction propagates from top to bottom of the reactant compact, and the reactants transform to the Fe-B alloy and Al₂O₃ where the combustion wave has passed. The adiabatic temperature (T_{ad}) of the combustion reaction (1) at 260 °C is calculated to be approximately 3400 °C [20, 21].

The XRD pattern of the Fe_{94.3}B_{5.7} alloy is shown in Fig. 1. The Fe_{94.3}B_{5.7} alloy displays the composition of *t*-Fe₂B and α -Fe phases; however, the metastable Fe₃B phase is not found. The strongest intensity ratio of the (110)_{*t*}/(002)_{*t*} of the Fe_{94.3}B_{5.7} alloy indicates that the predominant phase identified is the α -Fe phase. It is in accord with the result of the calculated phase diagram.

Figure 2 shows the SEM secondary electronic images of the Fe_{94.3}B_{5.7} alloy. The Fe_{94.3}B_{5.7} alloy is a composite structure of micrometer-sized dendrites dispersed in a eutectic matrix. The dendrite trunk thickness is about 5 μm , and the arm spacing of the dendrite is a few micrometers. The dendrite phase has tetragonal structure according to the phase identification by the selected area electron diffraction (SAED) analysis. The eutectic colonies

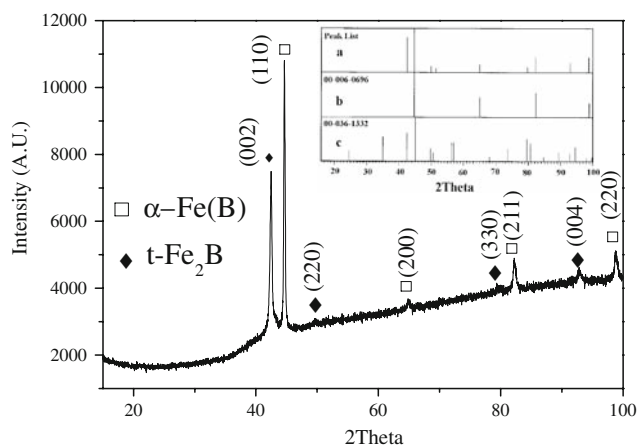


Fig. 1 The XRD pattern of the $\text{Fe}_{94.3}\text{B}_{5.7}$ alloy, inset (a) the experimental XRD pattern; (b) and (c) the standard XRD pattern of α -Fe and t - Fe_2B , respectively

distribute uniformly and the size is in the range 10–20 μm , and the content of the eutectic structure in the $\text{Fe}_{94.3}\text{B}_{5.7}$ alloy is about 70%.

The eutectic matrix microstructure cannot be resolved using SEM. The TEM observations of the $\text{Fe}_{94.3}\text{B}_{5.7}$ alloy are represented in Fig. 3. The nanostructured eutectic is found relatively disorganized (Fig. 3a). The TEM observations demonstrate that fine α/t phases inside the colonies are arranged in an alternating fashion. Figure 3b shows the high magnification of the zone I in the Fig. 3a. The corresponding SAED of the I zone (Fig. 3c) and the II zone (Fig. 3d) results confirm the existence of the two phases of the eutectic, α -Fe(B) and t - Fe_2B . Figure 3c also indicates that the precipitation t - Fe_2B is found in the α -Fe(B) phase.

Eutectic microstructures involve the simultaneous growth of two solid phases from the melt, which results from the cooperative growth of two crystalline phases by a discontinuous reaction. In this kind of process, there is no concentration difference across the reaction front, but short-range diffusion takes place paralleling to the reaction front and the two components separate into two different

phases. In a very high super-heating liquid state about 3400 $^{\circ}\text{C}$, the contaminants introduced from igniter are dissolved and purified in the metallic melt. Thus, the undercooling degree is greatly increased because there are no heterogeneous nucleation sites for the liquid to crystallize on. Crystal growth velocities of Fe and Fe_2B phases are a function of undercooling degree in the Fe-B binary alloy melt [24]. The growth velocity of the Fe_2B phase is always higher than that of the Fe phase, as boron content is below 15 at% in the Fe-B alloy under the large undercooling degree [22, 23]. So the effect of solute enrichment at the solid–liquid interface tends to increase the tip radius of the primary Fe_2B . This process will be persisted until the occurrence of stability of solute dendrites. Thus the dendrite phase has the t - Fe_2B structure rather than α -Fe(B) in the $\text{Fe}_{94.3}\text{B}_{5.7}$ alloy under the deeply super-cooling degree. The higher growth velocity of the Fe_2B phase also results in the breaking of the symmetry of lamella eutectic and leads to the formation of a hypereutectic structure ($\text{Fe}_2\text{B} + \text{eutectic}$). At the same time, the fine eutectic structure is formed because of the large degree of undercooling.

By the TEM analysis, it is found that solid/solid transformation takes place during the sample cooling. Taking the Fe–B binary phase diagram [24] into account, the γ -Fe(B) phase undergoes two solid/solid transformations. The formation of polycrystalline phase instead of a single crystal phase is attributed to the type of transformation. After the eutectic transformation, crystals of α -Fe(B) phase are nucleated within the γ -Fe(B) phase with decreases of the temperature [25]. The eutectoid transformation undergoes a similar process at 912 $^{\circ}\text{C}$. As the temperature, is decreased the B solid solution degree in the Fe is reduced, so the Fe_2B grains are precipitated in the α -Fe(B) phase (Fig. 3b).

In order to understand in detail the overall phase transformation process (i.e., solidification and solid-state transformation), complementary DSC analysis is performed for the $\text{Fe}_{94.3}\text{B}_{5.7}$ alloy. Typical DSC curves are shown in Fig. 4. For heating (curve (a)), three sharp

Fig. 2 SEM secondary electronic images of the $\text{Fe}_{94.3}\text{B}_{5.7}$ alloy, showing the eutectic and dendrite composite morphology

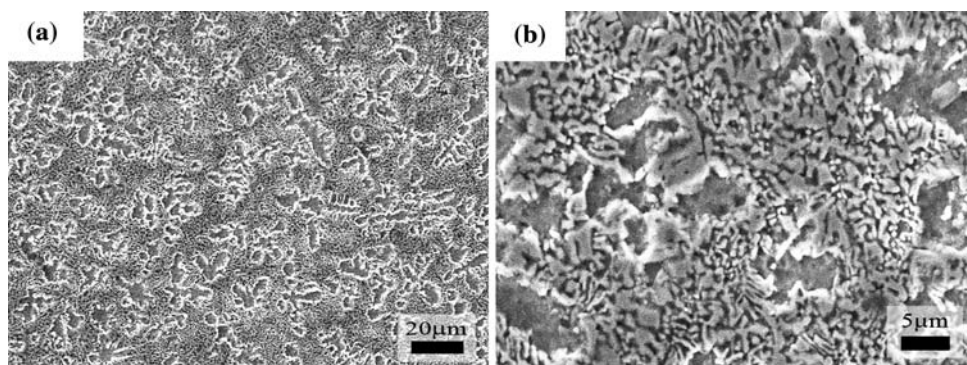
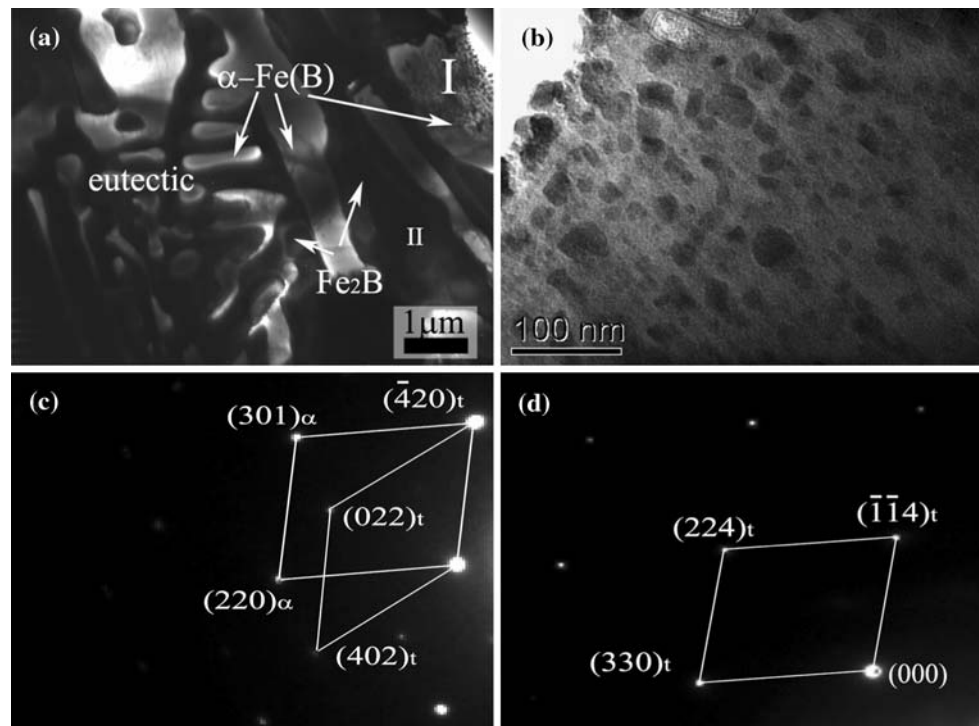


Fig. 3 Bright-field TEM images of the $\text{Fe}_{94.3}\text{B}_{5.7}$ alloy: (a) nanostructure eutectic colonies, (b) high magnification of zone I of (a), (c) corresponding SAED of the zone I, (d) corresponding SAED of the zone II



endothermic peaks (at about 1135, 1150, and 1212 °C) are observed. The first endothermic peak is associated with the solid solution transform temperature T_{ss} detected at 1135 °C in the solid state, and the second one with the eutectic melt temperature at 1150 °C. On further heating Fe_2B starts to melt at 1212 °C, resulting in the third peak. For cooling (curve (b)), three exothermic peaks (1134, 1171, and 1198 °C) occur as well, also corresponding to the T_{ss} , eutectic melt and Fe_2B melt temperatures, respectively.

Figure 5 displays that the coercive force (H_c) value of the $\text{Fe}_{94.3}\text{B}_{5.7}$ alloy is approximately 11 A/m and

saturation magnetization (M_s) is up to 1.74 T. It is well known that the microstructure essentially determines the hysteresis loop of a ferromagnetic material [26, 27]. The low H_c is attributed to the finest composite structure. The lamellar spacing of the eutectic is below 50 nm, and the interval of the precipitation grain is down to 20 nm. These values are less than the ferromagnetic change length, which is typically 40–50 nm in the Fe-B alloy. Thus, the lower coercivity is obtained. Also, we can see that the high saturation magnetization reaches 1.74 tesla because the content of Fe element reaches 94.3 wt% in the Fe-B alloy.

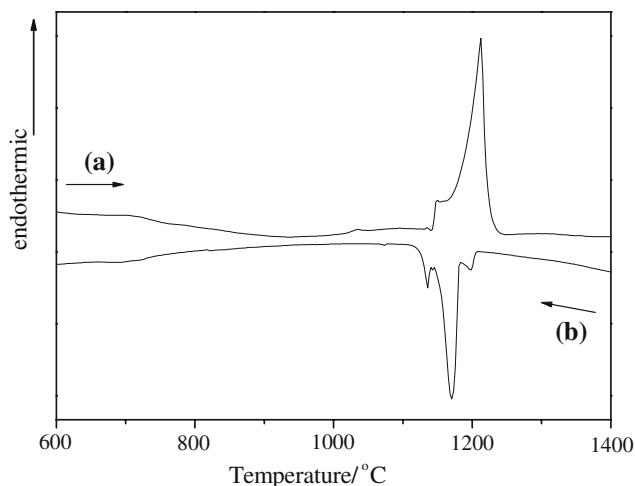


Fig. 4 DSC traces for the $\text{Fe}_{94.3}\text{B}_{5.7}$ alloy (heating curve (a) and cooling curve (b))

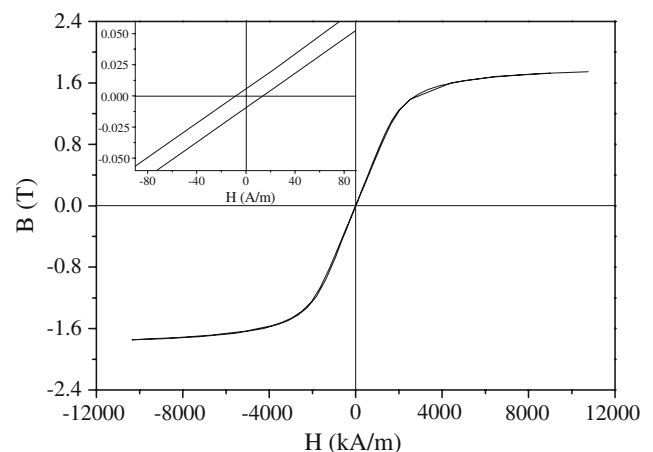


Fig. 5 Schematic of a magnetic hysteresis loop of the nanostructured $\text{Fe}_{94.3}\text{B}_{5.7}$ alloy; the inset shows expanded portions of the B-H curve

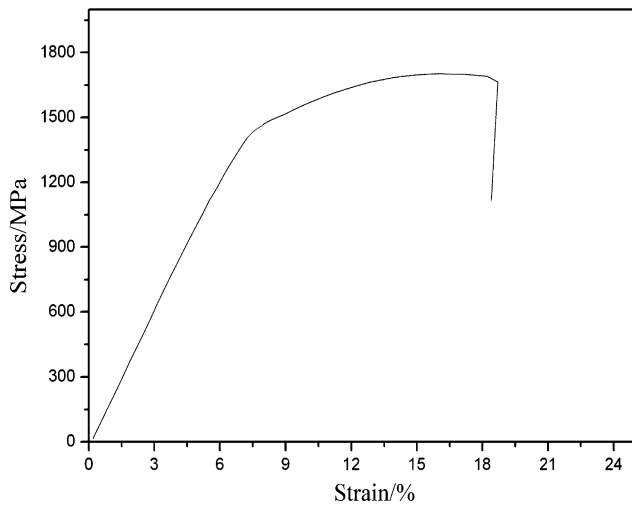


Fig. 6 Compressive engineering stress–strain curve of the $\text{Fe}_{94.3}\text{B}_{5.7}$ alloy

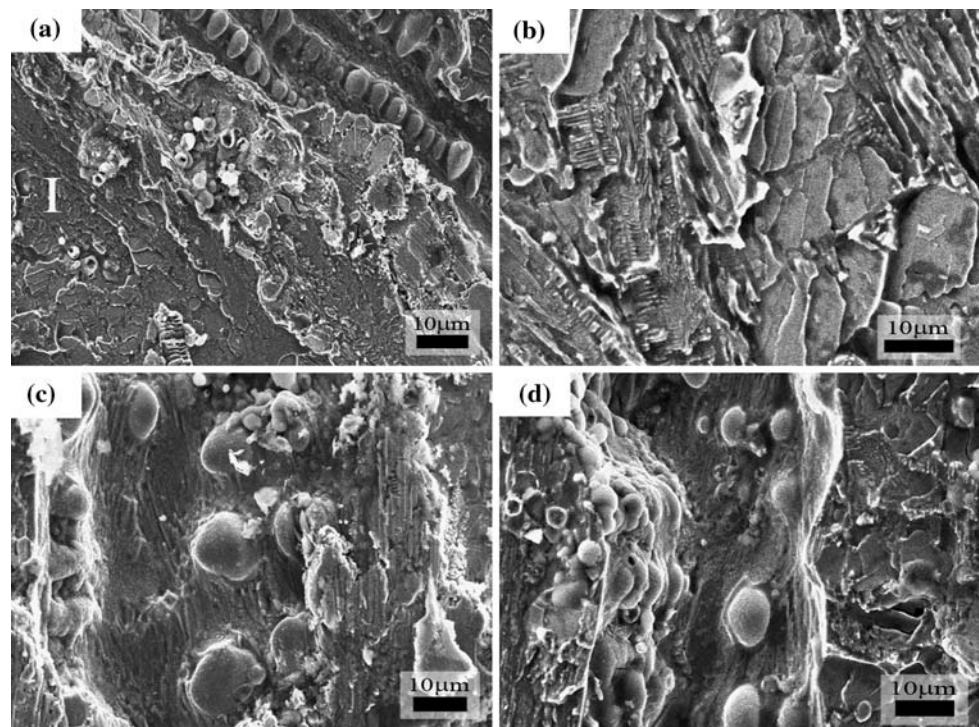
Figure 6 shows the compressive engineering stress–strain curve of the $\text{Fe}_{94.3}\text{B}_{5.7}$ alloy. The yield strength of 1430 MPa, and impressive ultimate strength of 1710 MPa and plastic strain of 19.8% are reached in compression, respectively. The yield strength is far higher than the reported 580 MPa of the coarse crystalline $\text{Fe}_{83}\text{B}_{17}$ alloy prepared by the traditional technique, and the plasticity strain retains a high value at the same time [28]. The $\text{Fe}_{94.3}\text{B}_{5.7}$ alloy presents a continuous stress increase with increasing strain, pointing to continuous work hardening until failure.

Figure 7a presents the typical features on the fracture surface of the $\text{Fe}_{94.3}\text{B}_{5.7}$ alloy, illustrating a visible shear fracture, which is usually generated by plastic deformation. The remelting evidence and flat fracture surface with distinct viscous shear flow traces are observed in Fig. 7b, indicating that shear bands induce a severe local energy transformation during the fracture of the sample, resulting in local temperature increase and local ‘softening’ of the alloy at the moment of fracture. The Fig. 7c and d demonstrates an obviously viscous shear flow phenomenon. Some shear bands propagate round the dendrite, and others are arrested near the intersection of the eutectic and dendrites. The eutectic colonies around the dendrites markedly rotate to accommodate the local stress deformation, which avoids catastrophic fracture due to the local stress concentration [29, 30]. The composite microstructure of the $\text{Fe}_{94.3}\text{B}_{5.7}$ alloy is responsible for continuous work hardening in the compressive deformation process, which results in the large plasticity.

Conclusions

In this work, we applied a simple and effective means (SHS Combining Rapid Cooling Technique) to prepare the bulk nanostructured hypoeutectic $\text{Fe}_{94.3}\text{B}_{5.7}$ alloy. The $\text{Fe}_{94.3}\text{B}_{5.7}$ alloy is characterized by a lamellar eutectic with $\epsilon\text{-Fe}_2\text{B}$ and $\alpha\text{-Fe}$ phases. The eutectic lamellar space is about 50 nm and the size of spherical eutectic colonies is in the

Fig. 7 Fracture surfaces of the $\text{Fe}_{94.3}\text{B}_{5.7}$ alloy from SEM, presenting shear bands typical for plastic deformation behavior: (a) fracture surface; (b) zone I high magnification; (c) and (d) depicting the shear bands origination or propagation from dendrite



range 3–25 μm . The nanostructured eutectic is attributed to deep undercooling. The $\text{Fe}_{94.3}\text{B}_{5.7}$ alloy displays good soft magnetic behavior with the coercive force (H_c) of 1.9 A/m and saturation flux density (B_s) of 1.75 T. The $\text{Fe}_{94.3}\text{B}_{5.7}$ alloy also exhibits simultaneously high yield strength (1430 MPa) and large plasticity ($\sim 19.8\%$), which is attributed to the nanostructured eutectic with a few micrometer dendrites of the composite $\text{Fe}_{94.3}\text{B}_{5.7}$ alloy. The shear bands induced in the eutectic matrix propagated is rounded or arrested by the dendrites. The SHS technique combined with rapid cooling technique can be used for tailoring nanostructured composite materials, which are expected to be applied to many sample alloy systems due to their extraordinary properties.

Acknowledgments This work was supported by the National Natural Science Foundation of China (50801064) and the Innovation Group Foundation from NSFC (50721062).

References

- M.A. Meyers, A. Mishra, D.J. Benson, *Prog. Mater. Sci.* **51**, 427 (2006). doi:10.1016/j.pmatsci.2005.08.003
- C.C. Koch, K.M. Youssef, R.O. Scattergood, K.L. Murty, *Adv. Eng. Mater.* **7**, 787 (2005). doi:10.1002/adem.200500094
- S.J. Koh, *Nanoscale Res. Lett.* **2**, 519 (2007). doi:10.1007/s11671-007-9091-3
- K.S. Kumar, H. Van Swygenhoven, S. Suresh, *Acta Mater.* **51**, 5743 (2003). doi:10.1016/j.actamat.2003.08.032
- L. Lu, Y. Shen, X. Chen, L. Qian, K. Lu, *Science* **304**, 422 (2004). doi:10.1126/science.1092905
- T. Kulik, *J. Non-Cryst. Solids* **287**, 145 (2001). doi:10.1016/S0022-3093(01)00627-5
- M.A. Meyers, A. Mishra, D.J. Benson, *Prog. Mater. Sci.* **51**, 427 (2006). doi:10.1016/j.pmatsci.2005.08.003
- G.P. Dinda, H. Rosner, G. Wilde, *Mater. Sci. Eng. A* **410–411**, 328 (2005). doi:10.1016/j.msea.2005.08.091
- H. Li, F. Ebrahimi, *Mater. Sci. Eng. A* **347**, 93 (2003). doi:10.1016/S0921-5093(02)00586-5
- R.Z. Valiev, R.K. Islamgaliev, I.V. Alexandrov, *Prog. Mater. Sci.* **45**, 103 (2000). doi:10.1016/S0079-6425(99)00007-9
- J.J. Moore, H.J. Feng, *Prog. Mater. Sci.* **39**, 243 (1995). doi:10.1016/0079-6425(94)00011-5
- T. Sriharan, S. Murali, *J. Mater. Process Technol.* **113**, 469 (2001). doi:10.1016/S0924-0136(01)00604-5
- J.A. Puszynski, in *Carbide*, ed. by A.W. Weimer (Chapman & Hall, London, 2002), p. 183
- R. Hasegawa, R. Ray, *J. Appl. Phys.* **49**, 4174 (1978). doi:10.1063/1.325328
- Y. Waseda, H.S. Chen, *Solid State Commun.* **27**, 809 (1978). doi:10.1016/0038-1098(78)90703-2
- T. Kemeny, I. Vincze, B. Fogarassy, *Phys Rev B* **20**, 476 (1979). doi:10.1103/PhysRevB.20.476
- T. Nakajima, E. Kita, H. Ino, *J. Mater. Sci.* **23**, 1279 (1988). doi:10.1007/BF01154591
- O.T. Inal, C.V. Robino, L. Keller, *J. Mater. Sci.* **16**, 3183 (1981). doi:10.1007/BF00540327
- J. Yang, J.Q. Ma, W.M. Liu, Q.L. Bi, Q.J. Xue, *Scr. Mater.* **58**, 1074 (2008). doi:10.1016/j.scriptamat.2008.02.001
- P.Q. La, J. Yang, D.J.H. Cockayne, W.M. Liu, Q.J. Xue, Y.D. Li, *Adv. Mater.* **18**, 733 (2006). doi:10.1002/adma.200501684
- J. Yang, P.Q. La, W.M. Liu, Y. Hao, *Mater. Sci. Eng. A* **382**, 8 (2004). doi:10.1016/j.msea.2004.03.095
- M. Palumbo, G. Cacciamani, E. Bosco, M. Baricco, *Intermetallics* **11**, 1293 (2003). doi:10.1016/S0966-9795(03)00171-7
- C. Yang, F. Liu, G. Yang, Y. Chen, N. Liu, J. Li, Y. Zhou, *Mater. Sci. Eng. A* **458**, 1 (2007). doi:10.1016/j.msea.2007.01.123
- T. Van Rompaey, K.C. Hari Kumar, P. Wollants, *J. Alloy Compd* **334**, 173 (2002)
- G. Shao, P. Tsakirooulos, *Acta Metall. Mater.* **42**, 2937 (1994). doi:10.1016/0956-7151(94)90391-3
- G. Herzer, in *Handbook of Magnetic Materials*, vol. 10, ed. by K.H.J. Buschow (Elsevier Science B.V., Amsterdam, 1997)
- H.J. Kim, J.B. Lee, Y.M. Kim, M.H. Jung, Z. Jaglicic, P. Umek, J. Dolinsek, *Nanoscale Res. Lett.* **2**, 81 (2007). doi:10.1007/s11671-006-9034-4
- J. Nowacki, L. Klimek, *J. Mater. Sci.* **27**, 3651 (1992). doi:10.1007/BF01151846
- S.R. Jian, *Nanoscale Res. Lett.* **3**, 13 (2008)
- Y.H. Lin, S.R. Jian, Y.S. Lei, P.S. Yang, *Nanoscale Res. Lett.* **3**, 71 (2008). doi:10.1007/s11671-008-9119-3